Applied Acoustics 156 (2019) 1–6

Contents lists available at ScienceDirect

Applied Acoustics

journal homepage: www.elsevier.com/locate/apacoust

Real-time interleaved photoacoustic and ultrasound imaging for guiding interventional procedures

Weicheng Zhang [a,b], Jiandong Li [a,b], Sihua Yang [a,b,*]

[a] MOE Key Laboratory of Laser Life Science & Institution of Laser Life Science, South China Normal University, Guangzhou 510631, China
[b] College of Biophotonics, South China Normal University, Guangzhou 510631, China

ARTICLE INFO

Article history:
Received 19 April 2019
Received in revised form 4 June 2019
Accepted 25 June 2019

Keywords:
Photoacoustic tomography
Ultrasound imaging
Transducer array
Clinical application

ABSTRACT

A real-time interleaved photoacoustic and ultrasound (PAUS) dual-modality imaging system with a handheld probe was developed, which integrated signal scanning, image reconstruction and display. The imaging scheme is one photoacoustic (PA) frame followed by one ultrasound (US) B-mode frame, and the frame rate can reach up to 20 Hz, which was limited by the repetition rate of the laser. The axial and lateral resolutions of PA imaging are measured to be ~231 μm and ~308 μm, respectively. As for US imaging, the axial and lateral resolutions are ~400 μm and ~600 μm. The real-time imaging capability of the dual-modality system was confirmed by imaging the cross section of a tube that formed three parallel segments and was injected with a moving ink solution. Furthermore, the PAUS guidance of interventional procedures in tumor animal model was carried out. The blood vessels of tumor and solid/liquid medicines were clearly visible, as well as the needle tip and shaft. Experimental results suggest that the PAUS system is able to give in-time feedback about the distribution of the applied medicines and track the needle during interventional procedures. Overall, the dual PAUS imaging can provide complementary information of tumor vasculature and tumor morphology at the same time and same location, which will be helpful for the clinical applications of needle guidance, image-guided therapy and tumor detection.

1. Introduction

PA imaging, combining both optical and US properties [1,2], is one of the most burgeoning biomedical imaging modalities based on the PA effect under thermal and stress confinement condition from absorbing structures such as blood vessels [3]. Upon the irradiation of a short-pulsed laser beam on the biological tissue surface, optical absorption ensues that generates wide bands of acoustic waves by transient thermoelastic expansion. Soon after, acoustic waves are detected by an US transducer that is either linear-array or single-element, and turn into electrical voltage signals followed by amplifiers and filters. Subsequently, the PA reconstruction unfolds via a certain PA beamforming algorithm. PA imaging complements US by having another one optical absorption as a contrast mechanism at spatial resolutions. Using intrinsic contrast such as haemoglobin or melanin, PA imaging can deliver both morphological and functional information. In addition, on condition that molecularly targeted exogenous contrast agents are used, molecular information can also be acquired [4–7]. PA imaging has been widely used not only in biomedical imaging, but also in non-invasive therapy.

As a popular prostate cancer treatment option which calls for eternal implantation of radioactive seeds into the prostate [8], brachytherapy seeds are used to deliver localized radiation. Implantation is implemented by means of metal guide needle insertion according to preestablished treatment plan. Acoustic shadowing from microcalcification, off-axis seed placement, and placement in specific regions of the prostate are some of the reasons [9]. Moreover, the acoustic signal by a brachytherapy seed is significantly dependent on its orientation, which was proved that the best choice to detect signals was the orientation with their long axis perpendicular to the beam [10]. Therefore, it is still difficult for US to visualize those small seeds [11]. Furthermore, neither CT nor MRI is the practical imaging technology that can be qualified for monitoring brachytherapy seed placement and therapeutic agent injection intraoperatively [12,13]. CT is likely to bring about the risk of radiation exposure and does not address complications caused by overdosing healthy tissue. MRI has the drawbacks of

* Corresponding author at: MOE Key Laboratory of Laser Life Science & Institution of Laser Life Science, South China Normal University, Guangzhou 510631, China.
E-mail address: yangsh@scnu.edu.cn (S. Yang).

https://doi.org/10.1016/j.apacoust.2019.06.028
0003-682X/

high cost and long-time consumption. During the past decades, photoacoustic tomography (PAT) has been proven to have great potential for identifying substances within deep biological tissue. PAT bears an attribute of high penetration depth similar to US imaging, and it has advantages of outstanding optical resolution and high speed [14–18]. In addition, metal holds an optical absorption that is orders of magnitude greater than tissue, thus offering superb contrast of metal with PA imaging. PA imaging of brachytherapy seed has been reported [19–21]. But the absence of the integrated linear-array probe comprised of fibre bundle and transducer apart from insufficient real-time ability made it hard to monitor the whole interventional procedures with a handheld probe. Additionally, these imaging approaches can not provide PA and US images at the same time and same location, thus making it difficult to be applied in clinical applications. Due to the dual-modality cost and complicacy in need of multi-channel data acquisition, one kind of device that can be integrated with commercial US platform is easier to success [22]. What is more, non-ionizing US guidance with real-time ability has been widely implemented [23–25]. It means a lot when a combined system improves the needle visualization and provides reliable visualization of small seeds with PAUS imaging at the same time and same location both in real-time. Such an ability will contribute to the improvement in the conformity with the dosimetric plan and intraoperatively dose optimization.

In this paper, we successfully developed a dual-modality imaging system adapted from a commercial US imaging system (Prodigy, S-sharp, Taiwan) to image a tube which formed three parallel segments and was injected with an incessantly moving ink solution. Next, in tumour animal model, we leveraged its real-time capacity to perform an imaging experiment of visualizing metallic seeds and therapeutic agent injection during interventional procedures. It is favourable and helpful for needle guidance, image-guided therapy and tumour detection.

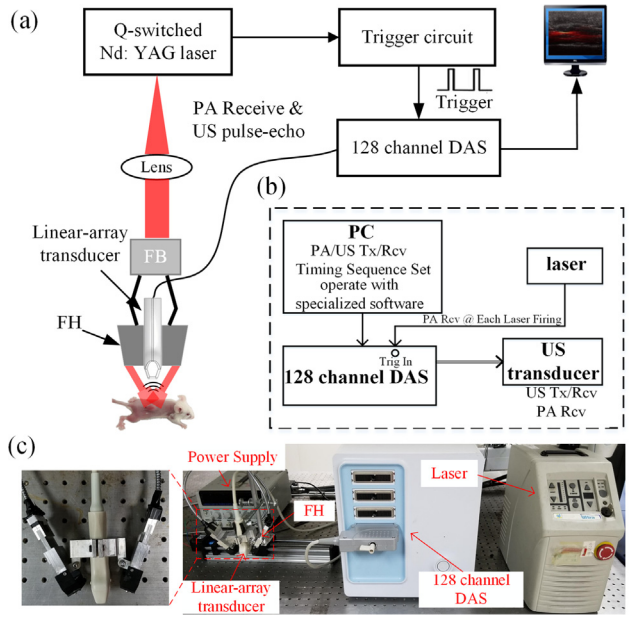

Fig. 1. Schematic diagram of the real-time interleaved PAUS imaging system. (a) Schematic of the experimental setup. FB: fibre bundle; FH: fibre holder. (b) Experimental timing sequence control block. The laser trigger synchronizes all events involved (laser firings, PA receiving). Tx: transmit; Rcv: Receive. (c) Photograph of the real-time interleaved PAUS imaging system.

2. Materials and methods

2.1. Experimental setup

Fig. 1 shows a schematic of the dual-modality PAUS integrated setup. A 128-element linear array US probe with a nominal bandwidth of 80% and a pitch of 200 μm (10 MHz, L14-6, Doppler, China) enclosed by a holder of a tailored bifurcated fibre bundle was used to detect both PA and US signals. In further descriptions, the axial and lateral refer to directions respectively parallel and perpendicular to the US probe beam axis. A Q-switched Nd:YAG laser (ULTRA, Big Sky Laser Tech, USA) with a pulse duration of 6 ns and a pulse repetition rate of 20 Hz at a wavelength of 1064 nm was employed as the laser source. Moreover, the single-pulse energy was configurable. Hence, we effectively controlled the fluence of 20 mJ/cm^2, well below safety limits 100 mJ/cm^2, at this wavelength [26]. Concerning *in vivo* PA imaging at a wavelength of 800 nm, a pulsed OPO (optical parameter oscillator) laser source (VIBRANT, OPOTEK Inc, USA) was also adopted. Light coupled into a 600 μm multimode fibre bundle from the laser was reshaped via a lens group, including a fibre collimator and an engineering diffuser. Two laser beams coming out of fibre bundle were rectangular in shape as the result of two cylindrical lenses. Besides, the fibre bundle was bifurcated and physically integrated with the US probe, which made it conducive with handheld photoacoustic imaging probe. The two optical beams were obliquely incident on the tissue surface with their angle adjustable. Indeed, these placements and configurations were to make sure that the incident plane of the light and the probe imaging plane intersected at the target depth. Dark-field illumination type was exploited here. On the tissue, it could be found that the interval of the two laser beams changed when adjusting the incident angle. It meant that the illumination area did not coincide with the detection area. Inside the tissue, owing to the scattering of laser, more photons would propagate into deeper area away from the tissue surface, which could minimize the surface interference signals and reduce their intensity compared to the signals in deeper area [27]. It was discovered that smaller incident angle, narrower separation interval and wider beams will leave more photons deposited right under the probe [28]. We thereby chose to form a narrow separation interval and wide beams since the effect of incident angle was minor. Here, a water tank was utilized to couple the US probe to the PAUS signals. Specifically, a 20 Hz frame rate was configured, with the laser pulse repetition rate set to 20 Hz.

2.2. System block diagram

A block diagram of the system that enunciates how to coordinate these components is presented in Fig. 1(b). A commercial ultrasound imaging system plays a major role as the platform of carrying out all data acquisition and reconstruction algorithm. First, the trigger of the laser is used to synchronize the PA signal recording with each laser firing instead of adopting a function generator. For interleaved dual-modality imaging, US pulse echoes are not in need of laser excitation, while laser excitation is necessary in PA. After each laser firing and PA signal recording, all the US pulse-echoes are activated. The transmitting US pulse has a centre frequency of 10 MHz, and the sampling frequency on receiving is 40 MHz. The detailed timing of PAUS signal acquisition and reconstruction is elaborated in Fig. 2. There is only one laser firing for PA receiving (128 channels for each laser firing) at each trigger cycle. Each laser firing and PA receiving is followed by 128 full beams of pulse-echo focused US. The parallel computation realization including raw data segmentation, PAUS beamforming, logarithmic

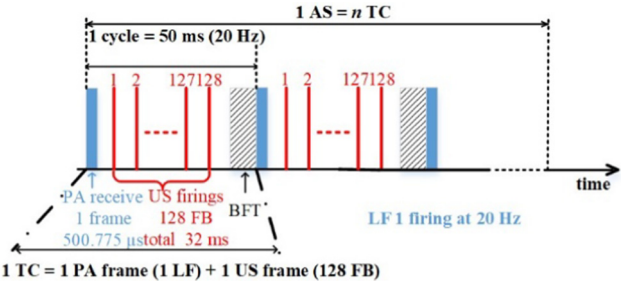

Fig. 2. Detailed timing diagram for interleaved PAUS real-time imaging system in continuous mode when PRF is set to 4 KHz. AS: acquisition set; TC: trigger cycle; LF: laser firings; BFT: beamforming and flush time; FB: full beams.

compression and image display, working along with a multicore GPU (GeForce GTX 750Ti, NVIDIA) allows real-time PAUS imaging display within the period of trigger cycle. The pattern results in a pair of interleaved PA and US images, while PA is a single-shot frame and a conventional B-mode US frame follows.

2.3. System detailed timing diagram

The detailed diagram about the coordination between PA and US in continuous mode is shown in Fig. 2. The time each US full beam takes is computed as the reciprocal of the pulse repetition frequency (PRF), which is identical to the time once PA signal recording takes. Typically, when PRF is set to 2 KHz, it takes 64 ms to finish 128 US full beams and 500 μs for each US full beam respectively. The time PA receiving takes is the product of event firing times and the period which corresponds to the PRF. Here, only one laser firing time is necessary for each frame real-time setting. One thing we should address is that there is a delay time (31 sampling time) when using external trigger. The entire time PA takes is usually considered to be 500.775 μs provided that the delay time is taken into our account. Also, the delay time should be included when performing PAUS beamforming in that it affects the delay time calculation of each scan-line. After finishing all the PAUS signal recording, the rest of time within each trigger cycle is taken to perform PA and US beamforming algorithm and image display. To further give an account of the process from raw data to photoacoustic/ultrasound image, a flowchart was given in Fig. 3.

2.4. Reconstruction algorithm

The filtered back-projection algorithm has been commonly taken due to the simple realization. In this study, we adopted a beamforming algorithm called delay-multiple-and-sum (DMAS), which was previously introduced by Lim et al. [29] in a study on RADAR imaging application for the detection of breast cancer. During the process of DMAS algorithm, the recording PA signals from different elements are combinatorially coupled, multiplied, and summed. Finally, the DMAS-beamformed signal can be obtain as

$$y_{DMAS}(t) = \sum_{i=1}^{N-1} \sum_{j=i+1}^{N} \hat{S}_{ij}(t), \tag{1}$$

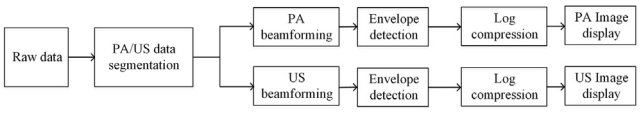

Fig. 3. The flowchart of the process from raw data to photoacoustic/ultrasound image.

where N is the number of elements of the linear array. Here, we derive a new signal by applying the signed square root to each $s_i s_j$ couple inside the summations

$$\hat{S}_{ij}(t) = \mathrm{sign}(s_i(t)s_j(t)) \times \sqrt{|s_i(t)s_j(t)|}. \tag{2}$$

In addition, the coherence factor is also used as a weighting coefficient to improve the quality. The CF can be written as

$$CF(t) = \frac{|\sum_{i=1}^{N} s_i(t)|^2}{N \times \sum_{i=1}^{N} |s_i(t)|^2}. \tag{3}$$

3. Results

We used two different reconstruction algorithms to compare the image of the cross section of a pencil lead with 0.5 mm diameter. As shown in Fig. 4, it is obvious that DMAS has a better performance. On the right side of these two images are their normalized PA intensity curve at the same depth. According to the full width at half maximum (FWHM) of these two algorithms, the FWHM of DMAS algorithm is narrower, ~0.693 mm while the FWHM of conventional delay-and-sum (DAS) is ~1.19 mm. With the purpose of spatial resolution measurement, a human hair inside a medium made up of 2% agar was made. Referring to the results in Fig. 5, 33 mm below the probe was a human hair with ~100 μm diameter. As we calculated, the lateral resolution is about 308 μm, and the axial resolution is about 231 μm which is superior to the other. As for the resolution measurement of US image, the same sample mentioned above was positioned 20 mm away from the probe surface, in that the acoustic beam width was the narrowest in the focus area of transmitting US waves. Using the same calculation method, it can be obtained that the US lateral resolution is about 600 μm and the axial resolution is about 400 μm. In order to further verify its imaging potential, two following experiments were also carried out.

One experiment is given in Fig. 6, which was intended to corroborate the real-time imaging capability. We carried it through by imaging the flowing ink solution within a taut tube. A low-density polyethylene (LDPE) transparent tube bearing an inner diameter of 2.5 mm was positioned in a water tank. And we twined it into three segments on purpose to test the ability of real-time imaging and rectangular illumination. When the laser beam fell on the tube, it could be inferred that PA image of different segments emerged gradually with the ink solution moving and permeating at various time points. Obviously, Fig. 6 shows that the frame rate of the imaging system can catch up with fast moving objects, without any segment missing. At first, both of the tube sides were not visible for the tube was empty in PA imaging and the tube was almost transparent to light, and their lower parts were also unseen

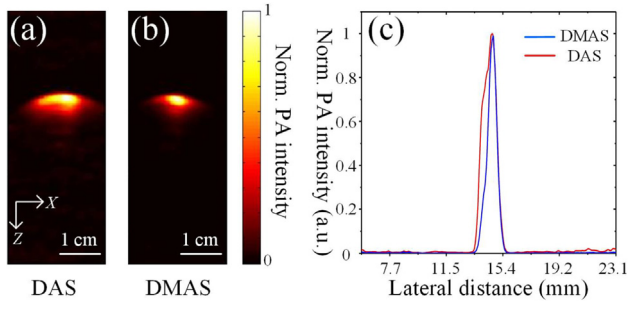

Fig. 4. Comparison between the two reconstructed PA images of a pencil lead at 20.7-mm depth using two different algorithms. (a) DAS algorithm, (b) DMAS. (c) Normalized PA intensity curves of the pencil lead with respect to lateral distance.

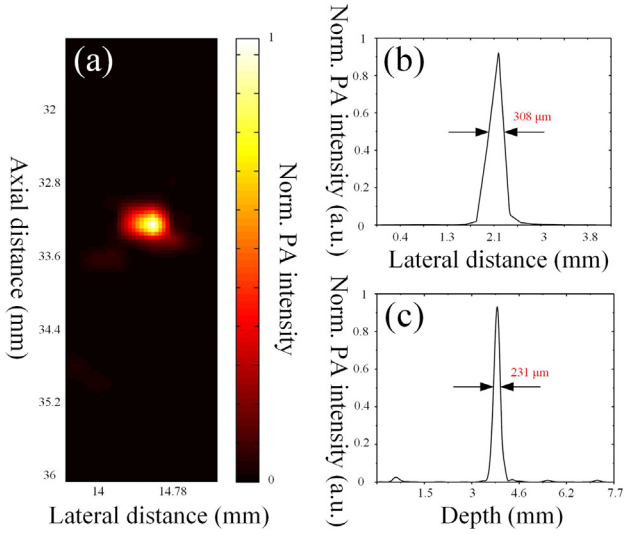

Fig. 5. Resolution calibration of the PAUS imaging system. (a) Reconstructed image of a human hair. (b) Lateral resolution. (c) Axial resolution.

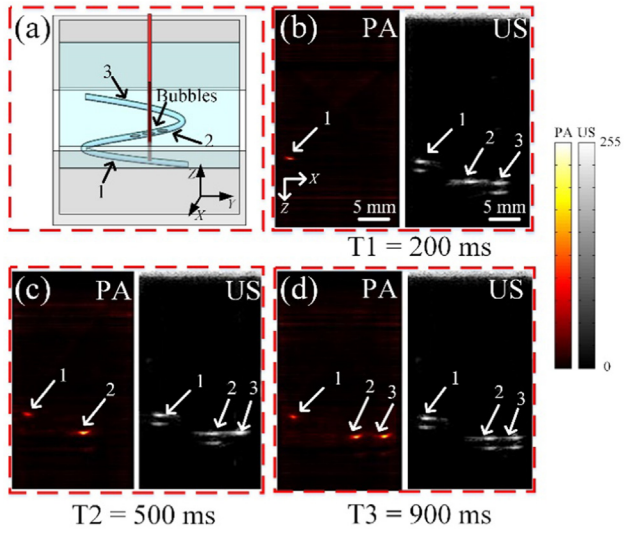

Fig. 6. The dynamics of filling the tube phantom with ink at different times chronologically. (a) Illustration of the tube that was twined into three segments. (b) One visible segment at first. (c) Two visible segments later. (d) All the three visible segments at last.

in US imaging on condition that the segment was empty. It can be seen that throughout the whole timespan, the first segment to permeate preceded the other two segments chronologically. At last, all the segments were visible in the PA and US image. Interestingly, the lower border of the second segment was unseen in the first US image, and that of the third segment was also unseen in the second US imaging, as there were some air bubbles existing in the second segment of the tube at first. With the moving of ink, the empty room came right below the third segment. Ultimately, all segments were full of ink. The result was identical to what it was supposed to be and thus validated its reasonableness. The PA imaging display dynamic range is 50 dB and that of the US imaging display is 60 dB, respectively. Another experiment without air bubbles was provided in supplementary Visualization at 20 frame per second.

To substantiate the imaging potential in tumour animal model for monitoring the injection of therapeutic agents and placements of metallic seeds in the context of mimicking the interventional procedures, we carried on another experiment in tumour animal model as shown in Fig. 7. In this experiment, an ink solution acted as the kind of therapeutic agent. A BALB/c mouse with a body weight of ~25 g was selected. Throughout the experiment, the mouse was anesthetized using general anaesthesia to keep it static. Fig. 7(a) is a photograph of the mouse with its fur shaven and chemically depilated before imaging. First, Fig. 7(b) shows that the PA imaging prior to needle insertion was finished under 800 nm laser irradiation of a pulsed OPO laser. At 800 nm illumination, blood is the predominant absorber in the tissue that accounts for most corresponding PA signals. In Fig. 7(b), information about rich blood vessels around the tumour region can be acquired from the PA image. And it can be seen that the blood vessels were shown in the form of scattered dots across the region of tumour. The US image of the same area was also captured as Fig. 7(c), which gave us a contour and shape of the tumour in a general way. The overlaid PA/US image of the tumour was given in Fig. 7(d), which delivered both the morphological and functional information. With a tilted angle of insertion, the needle shaft and tip at the centre of the tumour could be both visible in Fig. 7(e). In the following Fig. 7(f) and (g), the imaging of therapeutic agent injection together with metallic seed placement was demonstrated, which offered a clear location and distribution of the applied medicines with high contrast. At last, we calculated the normalized 8-bit pixel values of therapeutic agent and metallic seed as shown in Fig. 7(h). It turned

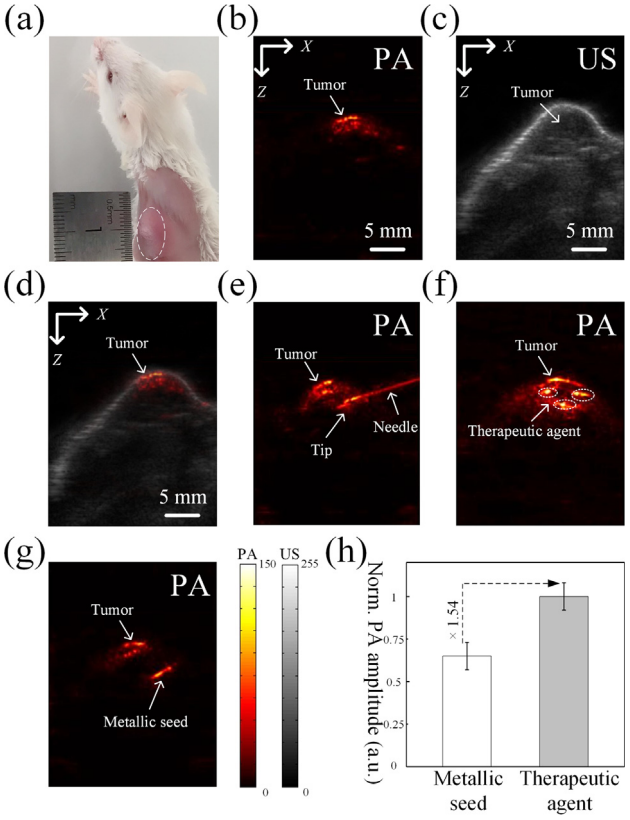

Fig. 7. The PAUS guidance of mimicking interventional procedures in tumour animal model, including metallic seed placement and therapeutic agent injection. (a) The photograph of the mouse with a tumour on its hinder back. (b) The PA B-scan imaging of the implanted tumour with plenty of blood vessel information. (c) The US B-mode imaging of the implanted tumour, indicating the size and contour. (d) The overlaid PA/US image showing both the morphological and functional information. (e) The PA imaging of monitoring needle insertion heading for the centre of the tumour, with its tip clearly visible. (f) The PA imaging after therapeutic agent injection. (g) The PA imaging after small metallic seed placement. (h) The normalized PA amplitude contrast of PA images between therapeutic agent and metallic seed.

out that the intensity of therapeutic agent was 1.54 times as strong as that of metallic seed.

4. Discussion

The real-time PAUS imaging system we developed was capable of presenting high contrast imaging of image-guided interventional procedures, which has the prospect of non-invasive screening, diagnosis and staging of cancer with more feasible application such as breast tumour, melanoma imaging. With respect to PA imaging in deep tissue, nanoparticles are commonly used to mark specific region with enhanced signals, which can also be accomplished easily using the real-time dual-modality system [30,31]. Further system developments, mostly focus on laser delivery and transducer performance optimization. Typically, a linear array-based PA imaging setup is comprised of a laser illumination system physically fixed on an US detector array and a data acquisition system for both PA and US signals. Given that commercially procurable US probes are not aiming at being specifically designed for PA signal receiving, there is still a challenge remaining that calls for custom-made sensitive and wide bandwidth transducers, which are optimal for PA signal receiving and not appropriate for US imaging [32]. In PAUS system, it is a compromise to opt for commercially available US probes. Besides, for fast scanning, there is a need to develop a US imaging system by use of a low cost, light weight laser diode, which makes it easier to handle [33]. Here, compensation of optical fluence was not taken into our consideration. This is part of our future work.

Currently, the frame rate is limited by the repetition rate of the laser. Adopting a laser with a higher repetition rate is part of the solution to the issue. Apart from this, more advanced US technologies can also be applied to the dual-modality system. US plane-wave imaging is a staple utilization of US ultrafast imaging. With coherent plane-wave compounding applied, the quality of US plane-wave imaging can be equal to that of conventional B-mode imaging, while US plane-wave imaging still possesses huge merits of ultrafast speed and less US transmitting beams. Of course, a number of ways to enhance the resolution and contrast of US imaging are also applicable [34–36].

5. Conclusion

In conclusion, we finished the development of a real-time interleaved dual-modality PAUS imaging system with a compact handheld probe. In addition, we successfully carried out the monitoring of therapeutic agent injection and metallic seed delivery into a tumour in real-time, as well as tracking needle. The combination of PAUS imaging can not only identify solid/liquid medicines with high contrast, but also provide their relative location to the tumours in animal models, which is of great help for needle guidance, image-guided therapy and tumour detection in terms of clinical applications.

Declaration of Competing Interest

None.

Acknowledgements

This work has been supported by the National Natural Science Foundation of China (61822505; 11774101; 61627827; 81630046; 91539127), the Science and Technology Planning Project of Guangdong Province (2015B020233016), and the Science and Technology Youth Talent for Special Program of Guangdong (2015TQ01X882).

Appendix A. Supplementary data

Supplementary data to this article can be found online at https://doi.org/10.1016/j.apacoust.2019.06.028.

References

[1] Zhang HF, Maslov K, Stoica G, Wang LV. Functional photoacoustic microscopy for high-resolution and noninvasive *in vivo* imaging. Nat Biotechnol 2006;24:848–51.
[2] Wang XD, Pang YJ, Ku G, Xie XY, Stocia G, Wang LV. Noninvasive laser-induced photoacoustic tomography for structural and functional *in vivo* imaging of the brain. Nat Biotechnol 2003;21:803–6.
[3] Yang DW, Xing D, Yang SH, Xiang LZ. Fast full-view photoacoustic imaging by combined scanning with a linear transducer array. Opt Express 2007;15:15566–75.
[4] Xie C, Upputuri PK, Zhen X, Pramanik M, Pu K. Self-quenched semiconducting polymer nanoparticles for amplified *in vivo* photoacoustic imaging. Biomaterials 2017;119:1–8.
[5] Sivasubramanian K, Mathiyazhakan M, Wiraja C, Upputuri PK, Xu C, Pramanik M. Near-infrared light-responsive liposomal contrast agent for photoacoustic imaging and drug release applications. J Biomed Opt 2017;22:041007.
[6] Gawale Y, Adarsh N, Kalva SK, Joseph J, Pramanik M, Ramaiah D, et al. Carbazole-linked near-infrared aza-BODIPY dyes as triplet sensitizers and photoacoustic contrast agent for deep-tissue imaging. Chem Eur J 2017;23:6570–8.
[7] Huang S, Upputuri PK, Liu H, Pramanik M, Wang M. A dual-functional benzobisthiadiazole derivative as an effective theranostic agent for near-infrared photoacoustic imaging and photothermal therapy. J Mater Chem B 2016;4:1696–703.
[8] Nag S, Beyer D, Friedland J, Grimm P, Nath R. American brachytherapy society (ABS) recommendations for transperineal permanent brachytherapy of prostate cancer. Int J Radiat Oncol 1999;44:789–99.
[9] Xue J, Waterman F, Handler J, Gressen E. Localization of linked ^{125}I seeds in postimplant TRUS images for prostate brachytherapy dosimetry. Int J Radiat Oncol 2005;62:912–9.
[10] Davis BJ, Kinnick RR, Fatemi M, Lief EP, Robb RA, Greenleaf JF. Measurement of the ultrasound backscatter signal from three seed types as a function of incidence angle: application to permanent prostate brachytherapy. Int J Radiat Oncol 2003;57:1174–82.
[11] Van Gellekom MPR, Moerland MA, Battermann JJ, Lagendijk JJW. MRI-guided prostate brachytherapy with single needle method-a planning study. Radiother Oncol 2004;71:327–32.
[12] D'Amico AV, Cormack R, Kumar S, Tempany CM. Real-time magnetic resonance imaging-guided brachytherapy in the treatment of selected patients with clinically localized prostate cancer. J Endour 2000;14:367–70.
[13] Westendorp H, Hoekstra CJ, Van't Riet A, Minken AW, Immerzeel JJ. Intraoperative adaptive brachytherapy of iodine-125 prostate implanted guided by C-arm cone-beam computed tomography-based dosimetry. Brachytherapy 2007;6:231–7.
[14] Wang LV, Yao JJ. A practical guide to photoacoustic tomography in the life sciences. Nat Methods 2016;13:627–38.
[15] Taruttis A, Ntziachristos V. Advances in real-time multispectral optoacoustic imaging and its applications. Nat Photonics 2015;9:219–27.
[16] Wang LV, Hu S. Photoacoustic tomography: in vivo imaging from organelles to organs. Science 2012;335:1458–62.
[17] Kim J, Park S, Jung Y, Chang S, Park J, Zhang Y, et al. Programmable real-time clinical photoacoustic and ultrasound imaging system. Sci Rep 2016;6:35137.
[18] Montilla LG, Olafsson R, Bauer DR, Witte RS. Real-time photoacoustic and ultrasound imaging: a simple solution for clinical ultrasound systems with linear arrays. Phys Med Biol 2013;58:N1–N12.
[19] Su JL, Bouchard RR, Karpiouk AB, Hazle JD, Emelianov SY. Photoacoustic imaging of prostate brachytherapy seeds. Opt Express 2011;2:2243–54.
[20] Harrison T, Zemp RJ. Coregistered photoacoustic-ultrasound imaging applied to brachytherapy. J Biomed Opt 2011;16:080502.
[21] Kuo N, Kang HJ, Song DY, Kang JU, Boctor EM. Real-time photoacoustic imaging of prostate brachytherapy seeds using a clinical ultrasound system. J Biomed Opt 2011;17:066005.
[22] Song KH, Kim C, Maslov K, Wang LV. Noninvasive in vivo spectroscopic nanorod-contrast photoacoustic mapping of sentinel lymph nodes. Eur J Radiol 2009;70:227–31.
[23] Natarajan S, Marks LS, Margolis D, Huang JT, Macairan ML, Lieu P, et al. Clinical application of a 3D ultrasound-guided prostate biopsy system. Urol Oncol 2011;29:334–42.
[24] Sauer G, Deissler H, Strunzz K, Helms G, Remmel E, Koretz K, et al. Ultrasound-guided large-core needle biopsies of breast lesions: analysis of 962 cases to determine the number of samples for reliable tumor classification. Br J Cancer 2005;92:231–5.
[25] McMillan AM, Landorf KB, Gilheany MF, Bird AR, Morrow AD, Menz HB. Ultrasound guided corticosteroid injection for plantar fasciitis: randomised controlled trial. BMJ 2012;344:e3260.
[26] Laser Institute of America 2000 American National Standards for the Safe Use of Lasers ANSI Z136.1

[27] Bai YY, Cong B, Gong XJ, Song L, Liu CB. Compact and low-cost handheld quasi bright-field linear-array probe design in photoacoustic computed tomography. J Biomed Opt 2018;23:121606.
[28] Wang GH, Zhao HH, Ren QS, Li CH. Simulation of light delivery for photoacoustic breast imaging using the handheld probe. Chin Opt Lett 2014;12:051703.
[29] Lim HB, Nhung NT, Li EP, Thang ND. Confocal microwave imaging for breast cancer detection: delay-multiple-and-sum image reconstruction algorithm. IEEE Trans Biomed Eng 2008;55:1697–704.
[30] Liu RA, Xiang LZ, Xing D, Li JD, Qin H, Zhang WC, et al. Large depth focus-tunable photoacoustic tomography based on clinical ultrasound array transducer. Appl Phys Lett 2018;113:141102.
[31] Nie LM, Chen M, Sun XL, Rong PF, Zheng NF, Chen XY. Palladium nanosheets as highly stable and effective contrast agents for in vivo photoacoustic molecular imaging. Nanoscale 2014;6:1271–6.
[32] Xia WF, Piras D, Van Hespen JCG, Van Veldhoven S, Prins C, Van Leeuwen TG, et al. An optimized ultrasound detector for photoacoustic breast tomography. Med Phys 2013;40:032901.
[33] Sivasubramanian K, Pramanik M. High frame rate photoacoustic imaging at 7000 frame per second using clinical ultrasound system. Biomed Opt Express 2016;7:312–23.
[34] Almualimi M, Wille ML, Langton ML. Potential for ultrasound transit time spectroscopy to improve axial resolution. Appl Acoust 2018;133:91–6.
[35] Leavens C, Willams R, Burns P, Sherar M. The use of phase codes in ultrasound imaging: SNR gain and bandwidth requirements. Appl Acoust 2009;70:1340–51.
[36] Huang QH, Lu MH, Zheng YP, Chi ZR. Speckle suppression and contrast enhancement in reconstruction of freehand 3D ultrasound images using an adaptive distance-weighted method. Appl Acoust 2009;70:21–30.